The Astrophysical Journal, 780:45 (13pp), 2014 January 1 doi:10.1088/0004-637X/780/1/45

VARIABILITY OF THE HIGH-VELOCITY OUTFLOW IN THE QUASAR PDS 456

J. N. Reeves[1,2], V. Braito[3], J. Gofford[1], S. A. Sim[4], E. Behar[5], M. Costa[1], S. Kaspi[5,6], G. Matzeu[1], L. Miller[7], P. O'Brien[8], T. J. Turner[2], and M. Ward[9]
[1] Astrophysics Group, School of Physical and Geographical Sciences, Keele University, Keele, Staffordshire ST5 5BG, UK; j.n.reeves@keele.ac.uk
[2] Center for Space Science and Technology, University of Maryland Baltimore County, 1000 Hilltop Circle, Baltimore, MD 21250, USA
[3] INAF-Osservatorio Astronomico di Brera, Via Bianchi 46, I-23807 Merate (LC), Italy
[4] School of Mathematics and Physics, Queen's University Belfast, Belfast BT7 1NN, UK
[5] Department of Physics, Technion, Haifa 32000, Israel
[6] School of Physics & Astronomy and the Wise Observatory, Tel-Aviv University, Tel-Aviv 69978, Israel
[7] Department of Physics, University of Oxford, Denys Wilkinson Building, Keble Road, Oxford OX1 3RH, UK
[8] Department of Physics and Astronomy, University of Leicester, University Road, Leicester LE1 7RH, UK
[9] Department of Physics, University of Durham, South Road, Durham DH1 3LE, UK
Received 2013 July 12; accepted 2013 November 1; published 2013 December 11

ABSTRACT

We present a comparison of two *Suzaku* X-ray observations of the nearby ($z = 0.184$), luminous ($L_{\rm bol} \sim 10^{47}$ erg s^{-1}) type I quasar, PDS 456. A new 125 ks *Suzaku* observation in 2011 caught the quasar during a period of low X-ray flux and with a hard X-ray spectrum, in contrast with a previous 190 ks *Suzaku* observation in 2007 when the quasar appeared brighter and had a steep ($\Gamma > 2$) X-ray spectrum. The 2011 X-ray spectrum contains a pronounced trough near 9 keV in the quasar rest frame, which can be modeled with blueshifted iron K-shell absorption, most likely from the He- and H-like transitions of iron. The absorption trough is observed at a similar rest-frame energy as in the earlier 2007 observation, which appears to confirm the existence of a persistent high-velocity wind in PDS 456, at an outflow velocity of 0.25–0.30c. The spectral variability between 2007 and 2011 can be accounted for by variations in a partial covering absorber, increasing in covering fraction from the brighter 2007 observation to the hard and faint 2011 observation. Overall, the low-flux 2011 observation can be explained if PDS 456 is observed at relatively low inclination angles through a Compton-thick wind, originating from the accretion disk, which significantly attenuates the X-ray flux from the quasar.

Key words: black hole physics – quasars: individual (PDS 456) – X-rays: galaxies

Online-only material: color figures

1. INTRODUCTION

Outflows are an important phenomenon in active galactic nuclei (AGNs) and can play a key role in the co-evolution of the massive black hole and the host galaxy. Black holes grow by accretion and strong nuclear outflows can quench this process by effectively shutting off the supply of matter. Thus, outflows can provide feedback between the growth of the galactic bulge and the black hole (Silk & Rees 1998; King 2003; Di Matteo et al. 2005; McQuillin & McLaughlin 2012). Recently, a number of high column density ($N_{\rm H} \sim 10^{23}$ cm^{-2}), fast ($>0.1c$) outflows have been found in luminous AGNs, through observations of blueshifted absorption from Fe K, at rest-frame energies greater than 7 keV (e.g., Reeves et al. 2003, 2009; Pounds et al. 2003; Chartas et al. 2003; Tombesi et al. 2010, 2011; Gofford et al. 2013). These fast outflows may be driven off the accretion disk by either radiation pressure (Proga et al. 2000; Sim et al. 2010b) or by magnetorotational forces (Kato et al. 2004; Kazanas et al. 2012; Fukumura et al. 2010), or both, a few gravitational radii ($R_{\rm g}$) from the black hole. Under the assumption of a quasi-spherical outflow, then the outflow rates derived can be huge, of the order of several solar masses per year (Reeves et al. 2009; Tombesi et al. 2011), equivalent to 10^{45}–10^{46} erg s^{-1} in kinetic power. Such outflows are a likely consequence of near-Eddington accretion (King & Pounds 2003).

PDS 456 is a luminous, low-redshift ($z = 0.184$), radio-quiet quasar identified in 1997 (Torres et al. 1997). The optical and infrared spectra (Simpson et al. 1999) show broad Balmer and Paschen lines (e.g., H$\beta \sim 3000$ km s^{-1} FWHM), strong Fe II, a hard (de-reddened) optical continuum ($f_\nu \propto \nu^{-0.1\pm0.1}$), and one of the strongest "big blue bumps" of any AGN (Simpson et al. 1999; Reeves et al. 2000). It has a de-reddened, absolute magnitude of $M_B \approx -27$, making it at least as luminous as the radio-loud quasar 3C 273, with a bolometric luminosity of $L_{\rm bol} = 10^{47}$ erg s^{-1} (Simpson et al. 1999; Reeves et al. 2000), making PDS 456 one of the most luminous known quasars in the local universe.

A 2001 40 ks *X-ray Multi-Mirror Mission (XMM)-Newton* observation of PDS 456 revealed the presence of strong iron K-shell absorption above 7 keV, which could be attributed to a high-velocity outflow (Reeves et al. 2003), requiring a large column density of highly ionized matter. Furthermore, a strong, broad absorption line at 1 keV was observed in the Reflection Grating Spectrometer (also see Behar et al. 2010). A *Suzaku* observation in 2007 revealed the presence of two highly significant absorption lines observed at 7.68 and 8.15 keV (Reeves et al. 2009, hereafter R09), corresponding to 9.08 and 9.66 keV in the quasar rest frame, where no strong atomic transitions are expected. The observed energy of the absorption does not coincide with the expected position of the Fe XXV or Fe XXVI resonant ($1s - 2p$) absorption lines at $z = 0$ (at 6.7 or 6.97 keV) and therefore cannot be associated with local hot gas, such as the WHIM (McKernan et al. 2005).

Thus, a plausible identification of the absorption lines is with the strong resonance ($1s - 2p$) transitions of highly ionized iron, either Fe XXV or Fe XXVI, but blueshifted, with an implied outflow velocity of 0.25–0.30c. A column density of $N_{\rm H} \sim 5 \times 10^{23}$ cm^{-2} was also required to model the

large equivalent widths (∼100 eV) of the lines (R09). Even a conservative 10% global covering for the ionized outflow implies a mass outflow rate of $>10\ M_{\odot}\ \mathrm{yr}^{-1}$, similar to the expected mass accretion rate of PDS 456 (Reeves et al. 2003). PDS 456 also exhibits blueshifted absorption in the ultraviolet (UV; O'Brien et al. 2005), as seen in the form of a broad absorption trough blueward (by 12000–15000 km s^{-1}) of the Lyα emission line, as well as blueshifted C IV emission (by 5000–6000 km s^{-1}).

PDS 456 also has a record of showing long-term spectral variability over the last decade of observations (R09; Behar et al. 2010). Indeed, in an analysis of all the archived observations of PDS 456, Behar et al. (2010) showed that the complex variability was likely due to both absorption changes and variations in the intrinsic continuum level, while a relatively invariant ionized reflection component may also be superimposed on the spectra. In some of the observations, the quasar appeared to be highly absorbed, such as in the 2001 *XMM-Newton* observations (Reeves et al. 2003), while in the 2007 *XMM-Newton* observations the quasar appeared to be relatively continuum-dominated with little intrinsic X-ray absorption (Behar et al. 2010). The overall picture of spectral variability is likely complex, with intrinsic quasar X-ray variability occurring along with the changes in a possible partial covering absorber.

Here, we present a comparison between a 2007 and a more recent 2011 *Suzaku* observation of PDS 456. The original 2007 *Suzaku* observation revealed a steep unabsorbed continuum with photon index $\Gamma > 2$, as well as the presence of highly blueshifted absorption lines at 9 keV in the quasar rest frame. In contrast, the 2011 observation caught the quasar at a substantially lower flux and with a subsequently harder X-ray spectrum. In this paper, we present the comparison between the 2007 observation and the 2011 low-flux spectrum and subsequently show that the high-velocity outflow is persistent in both the 2007 and 2011 data sets at self-consistent velocities. Furthermore, in the 2011 observation, the X-ray spectrum is more likely dominated by reprocessed radiation, possibly from an accretion disk wind. Values of $H_0 = 70$ km s^{-1} Mpc^{-1} and $\Omega_{\Lambda_0} = 0.73$ are assumed throughout and errors are quoted at 90% confidence ($\Delta\chi^2 = 2.7$), for 1 parameter of interest.

2. *SUZAKU* OBSERVATIONS OF PDS 456

PDS 456 was first observed by *Suzaku* (Mitsuda et al. 2007) between 2007 February 24 and March 1 over a total duration of 370 ks and with a net (X-Ray Imaging Spectrometer, XIS) exposure time of 190 ks after screening. PDS 456 was subsequently re-observed by *Suzaku* between 2011 March 16–19 for a duration of ∼240 ks, with a corresponding next (XIS) exposure of 125.6 ks. Both observations were taken with PDS 456 at the aim-point of the XIS CCD cameras, otherwise known as the XIS nominal mode. A summary of the observations is shown in Table 1. The data were analyzed from the XIS (Koyama et al. 2007) and the PIN diodes of the Hard X-ray Detector (HXD/PIN; Takahashi et al. 2007) and processed using v2 of the *Suzaku* pipeline. Data were excluded within 436 s of passage through the South Atlantic Anomaly and within Earth elevation angles or Bright Earth angles of $<5^{\circ}$ and $<20^{\circ}$, respectively.

2.1. XIS Analysis

XIS data for both observations were selected in 3×3 and 5×5 editmodes using grades 0, 2, 3, 4, and 6, while hot and flickering pixels were removed using the SISCLEAN script. Spectra were (re)-extracted from within circular regions with a 1.′5 radius, while the background was taken from an annulus with a 3.6–6.′5 radius centered on the AGN, but which was free of any background sources. We also checked an alternate background subtraction method, whereby background spectra were extracted from four circles offset from the source and avoiding the chip corners containing the calibration sources. Both methods gave identical results, however we adopted the annulus method as that provided a greater background area and a more even sampling of the background across the CCDs. The subsequent background spectra were scaled down by a factor of $\times 0.075$ to match the size of the extraction region for the AGN.

The response matrices (RMF) and ancillary response (ARFS) files were created using the tasks XISRMFGEN and XISSIMARFGEN, respectively, the former accounting for the CCD charge injection and the latter accounting for the hydrocarbon contamination on the optical blocking filter. Spectra from the two front-illuminated XIS 0 and XIS 3 chips in both observations were combined to create a single source spectrum (hereafter XIS–FI) for each observation, while data from the back-illuminated XIS 1 chip were analyzed separately. Data were included from 0.6–10 keV for the XIS–FI and 0.6–7 keV for the XIS 1 chip. As the latter is mainly optimized for the soft X-ray band and has a higher background yet a small effective area in the iron *K*-band, we concentrate our analysis here on the XIS–FI spectra. However, we note that the XIS 0, XIS 1 and XIS 3 spectra are consistent with each other, for each observation (e.g., see R09 for a comparison for the 2007 observation).

The net background subtracted source count rates per XIS–FI CCD were 0.268 ± 0.001 counts s^{-1} (2007), and 0.139 ± 0.001 counts s^{-1} (2011), while the XIS background rates correspond to only 2.4% and 3.7% of the net source counts for the 2007 and 2011 observations, respectively. The net exposure per XIS–FI CCD for each observation was 190.6 ks and 125.6 ks, respectively. The XIS spectra and response files were subsequently binned to a minimum energy width corresponding to approximately the HWHM XIS resolution of 60 eV at 6 keV, dropping to ∼30 eV at lower energies. Channels were additionally grouped to a minimum of 40 counts per energy bin and χ^2 minimization was used for all subsequent spectral fitting.

2.2. HXD Analysis

The extraction of spectra from the non-imaging HXD/PIN instrument (Takahashi et al. 2007) is described in detail in R09 for the 2007 *Suzaku* observation of PDS 456. The same method is applied here to the 2011 observation. Spectra were re-extracted for both observations over the 15–50 keV range, while the background spectra were extracted from background model D (as described previously in R09), together with the predicted cosmic X-ray background (CXB) component, using the CXB spectrum and intensity as measured by Gruber et al. (1999). The net exposures obtained for the HXD/PIN are summarized in Table 1. The net source rates obtained for PDS 456 were low, $(1.6 \pm 0.3) \times 10^{-2}$ counts s^{-1} and $<4.5 \times 10^{-3}$ counts s^{-1} for 2007 and 2011 observations, respectively. These net count rates represent 3.3% and <1.1% of the total background count rate, while the systematic uncertainty of the background-D model is believed to be typically ±1.3% at the 1σ level for a net 20 ks exposure (Fukazawa et al. 2009). Thus, PDS 456 is not detected by HXD/PIN in the subsequent low-flux 2011 observation and is marginally detected during the 2007 observation, as discussed in detail by R09.

Table 1
Summary of PDS 456 *Suzaku* Observations

Instrument	Year	Start Date/Time[a]	End Date/Time[a]	Exposure[b]	$F_{0.5-2}$[c]	F_{2-10}[d]	F_{15-50}[e]
XIS	2007	2007 Feb 24 17:58	2007 Mar 1 00:51	190.6	3.46	3.55	...
HXD/PIN	2007	...	...	164.8	...	...	5.7 ± 2.2
XIS	2011	2011 Mar 16 15:00	2011 Mar 19 08:33	125.6	1.36	2.84	...
HXD/PIN	2011	...	...	93.6	...	...	<2.5

Notes.
[a] Observation start/end times are in UT.
[b] Net exposure time, after screening and deadtime correction, in ks.
[c] Observed flux in the 0.5–2 keV band, units $\times 10^{-12}$ erg cm^{-2} s^{-1}.
[d] Observed flux in the 2–10 keV band, units $\times 10^{-12}$ erg cm^{-2} s^{-1}.
[e] Observed flux in the 15–50 keV band, units $\times 10^{-12}$ erg cm^{-2} s^{-1}.

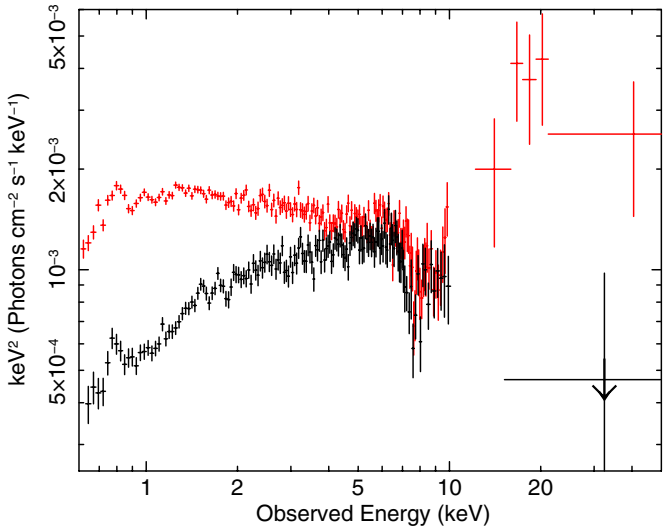

Figure 1. Fluxed spectra of PDS 456, unfolded against a simple $\Gamma = 2$ power law. The *Suzaku* XIS 03 and HXD/PIN spectra from 2007 (red) and 2011 (black) are plotted against observed energy. Below 10 keV, the XIS spectrum from 2011 is substantially harder compared with the 2007 data. Above 15 keV, PDS 456 is not detected in the HXD/PIN band during 2011, compared with 2007 where a strong hard X-ray excess is observed. Also, note the drop in flux in the iron *K* band above 7 keV in both observations.

(A color version of this figure is available in the online journal.)

In the subsequent spectral analysis of PDS 456 presented in Sections 3 and 4, we concentrate mainly on the properties of the XIS spectra below 10 keV, however we do perform consistency checks of the different spectral models by comparing the predicted model fluxes in the hard X-ray 15–50 keV band with the measurements or upper limits deduced during the 2007 and 2011 HXD data sets.

3. SPECTRAL ANALYSIS

Figure 1 shows the overall broadband fluxed spectra from 0.6–50 keV of both observations. Note that the spectra have been unfolded through the instrumental response against a simple $\Gamma = 2$ power-law model and are not corrected for Galactic absorption. Below 10 keV, the 2011 observation is clearly harder and shows continuum curvature down toward the lowest energies, which as discussed below may be the signature of substantial absorption. In contrast, the 2007 spectrum is largely power-law like below 10 keV and appears softer compared with a photon index of $\Gamma = 2$ in Figure 1.

Above 10 keV, the 2007 observation shows a clear hard excess in the HXD data, as was originally presented in R09, while the 2011 observation shows no such excess. However, including the systematic uncertainty in the HXD background level, then the relative 15–50 keV fluxes (computed from a $\Gamma = 2$ power law in the HXD band) are $(5.7 \pm 2.2) \times 10^{-12}$ erg cm^{-2} s^{-1} (2007) versus $<2.5 \times 10^{-12}$ erg cm^{-2} s^{-1} (2011), which are formally not consistent with being constant at the 90% level. However, given the possible uncertainties in modeling the non-X-ray background level of the HXD, we do not consider the hard X-ray variability further in this paper. More sensitive imaging hard X-ray observations above 10 keV, such as with *NuSTAR*, are required to probe this variability further. Nonetheless, we also note that such hard excesses above 10 keV are proving to be relatively common, occurring in a high fraction of even type I AGNs (Tatum et al. 2013).

For the remainder of the spectral analysis, we concentrate on the XIS–FI data below 10 keV, which have a very low background level. To simply parameterize the spectral differences below 10 keV, we started by fitting both observations simultaneously with a broken power-law model. Galactic absorption of $N_{\rm H} = 2 \times 10^{21}$ cm^{-2} (Dickey & Lockman 1990; Kalberla et al. 2005) was adopted, modeled with the "Tuebingen–Boulder" absorption model (TBABS in XSPEC) using the cross-sections and abundances of Wilms et al. (2000). The 2007 spectrum is very steep, with soft- and hard-band photon indices of $\Gamma = 3.16 \pm 0.07$ and $\Gamma = 2.33 \pm 0.02$ with a break energy of 1.09 ± 0.05 keV. In contrast, in 2011, the soft- and hard-band photon indices are $\Gamma = 2.48 \pm 0.12$ and $\Gamma = 1.85 \pm 0.02$, with the break energy tied to the above value. The relative soft- and hard-band fluxes derived from this model are also quoted in Table 1.

Nonetheless, the fit to the data with such a simple model is very poor, with $\chi^2_\nu = 680/314$, where there are 314 degrees of freedom in the fit. The model also does not fit the pronounced spectral curvature present in 2011, as seen in Figure 1. Indeed, Figure 2 shows the comparison between the two data sets, plotted as a ratio to the absorbed broken power law with the spectral parameters equal to the 2007 data set. In addition to the harder shape of the 2011 observation, a pronounced spectral drop is observed above 8 keV in the quasar rest frame, in the iron *K* band. Furthermore, possible excess emission is also observed around 0.9–1.0 keV, close to the expected energies for Ne IX or L-shell Fe, as detected previously in this AGN (R09).

3.1. Iron K-Band Absorption

Initially, we fit both observations with a simple power-law continuum model over the 2–10 keV band, modified by Galactic absorption, and allowed the relative photon indices and continuum normalizations to vary for each data set. Figure 3 shows

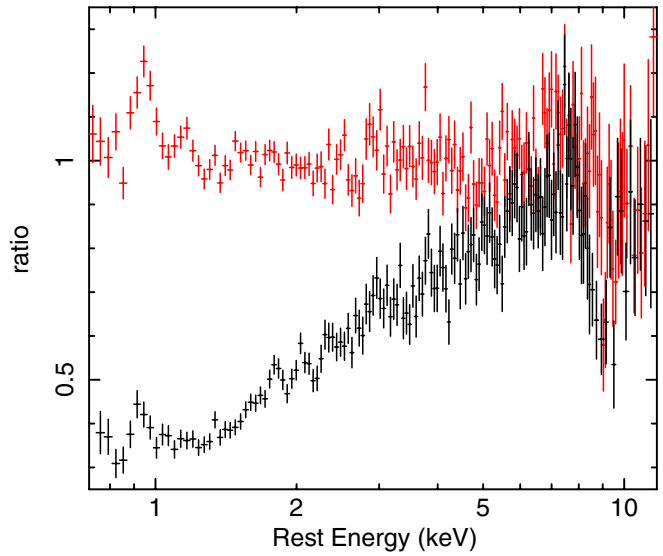

Figure 2. 2011 *Suzaku* XIS spectrum of PDS 456 (black) compared with the 2007 XIS spectrum. The data are plotted as a ratio to the broken power-law continuum model fit to the 2007 data, as described in the text. The spectra are plotted in the rest frame of PDS 456 (at $z = 0.184$). Note the strong Fe *K*-band absorption above 8 keV in the rest frame, which is especially apparent in the 2011 observation.

(A color version of this figure is available in the online journal.)

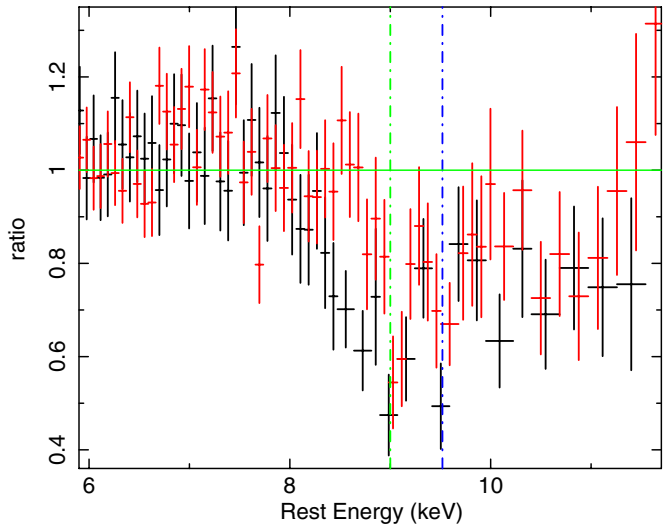

Figure 3. Data/model ratio in the Fe *K* band for the 2011 (black) and 2007 (red) observations. Note that the absorption profile is centered at a similar rest frame energy in both observations, however the 2011 absorption profile appears broader and extended redward, below 9 keV. The dot–dashed vertical lines are shown as a guide to represent the centroid energies of the absorption in the 2007 observation.

(A color version of this figure is available in the online journal.)

the data/model ratio residuals at iron K for both observations, plotted in the quasar rest-frame. Indeed, the absorption appears to be present in both observations at a self consistent energy between the observations, ruling out the possibility that the iron *K*-band absorption is due to statistical noise. Similar to what was reported by R09 in the analysis of the 2007 data set, the absorption could consist of two profiles, centered at 9.0 and 9.5 keV, respectively, in the quasar rest-frame or alternatively a single broad profile. One apparent difference is that the absorption profile in the 2011 observation appears to extend to lower energies between 8–9 keV.

Table 2
Gaussian Iron K Absorption Line Parameters

Component	Parameter	2007 Values	2011 Values	$\Delta\chi^2$ [a]
Line 1	Energy (keV)	9.06 ± 0.05	8.77 ± 0.14	124.3
	σ (keV)	$0.12^{+0.10}_{-0.08}$	$0.42^{+0.33}_{-0.12}$	
	Flux[b]	$-(3.2 \pm 0.8) \times 10^{-6}$	$-(9.7 \pm 2.2) \times 10^{-6}$	
	EW[c] (eV)	-129 ± 32	-370 ± 84	
Line 2	Energy (keV)	9.54 ± 0.06	[d]	37.6
	σ (keV)	0.1[e]	0.1[e]	
	Flux[b]	$-(2.5 \pm 0.9) \times 10^{-6}$	$-(3.2 \pm 1.2) \times 10^{-6}$	
	EW[c] (eV)	-121 ± 44	-156 ± 59	
Line 3	Energy (keV)	10.5 ± 0.2	[d]	36.9
	σ (keV)	>0.3	[d]	
	Flux[b]	$-(3.3 \pm 1.6) \times 10^{-6}$	$-(5.8 \pm 2.0) \times 10^{-6}$	
	EW[c] (eV)	-180 ± 87	-296 ± 102	
Power law	Γ	2.23 ± 0.03	1.84 ± 0.04	
	Flux[f]	3.55	2.77	

Notes.
[a] Improvement in χ^2 upon adding a component to the model.
[b] Line flux in units of photons cm^{-2} s^{-1}.
[c] Absorption line equivalent width.
[d] Parameter is tied between 2007 and 2011 spectra.
[e] Parameter fixed in model.
[f] Continuum flux in the 2–10 keV band, units $\times 10^{-12}$ erg cm^{-2} s^{-1}.

To quantify its properties, we parameterized the iron *K*-band absorption with simple Gaussian profiles, fitting two Gaussians lines to the apparent absorption lines at 9 and 9.5 keV. In addition, it was also found that an additional broad absorption trough was required at a rest frame energy above 10 keV, which may for instance represent an unresolved blend of high-order transitions or bound-free edges of iron. The properties of the absorption lines are summarized in Table 2. Adding the absorption profiles considerably improved the fit statistic compared with the baseline power-law model, which decreased from $\chi^2_\nu = 410/226$ (formally rejected with a null probability of 9×10^{-13}), to an acceptable $\chi^2_\nu = 211/215$ upon the addition of the absorption lines. Thus, the detection of the Fe *K*-band absorption from a statistical sense appears robust, appearing in the same band in both independent data sets. In addition, R09 also showed that the detection of the absorption in the 2007 observations was significant at >99.99% from Monte Carlo simulations, while in a systematic analysis of a sample of iron *K*-band absorbers in AGNs, Gofford et al. (2013) also found that the iron K absorption profiles in both the 2007 and 2011 observations of PDS 456 are significant at >99.9% confidence according to Monte Carlo simulations.

The main change in the absorption profile between the two observations is that the 9 keV absorption line appears centered toward lower energies in 2011, at 8.77 ± 0.14 keV versus 9.06 ± 0.05 keV in 2007, as indicated by Figure 3. Furthermore, the line profile appears to be resolved in 2011 (as can be seen by the extended absorption profile below ~9 keV), with a line width of $\sigma = 0.42^{+0.33}_{-0.12}$ keV, while in 2007 the profile of the 9 keV trough is barely resolved compared with the instrumental resolution ($\sigma = 0.12^{+0.10}_{-0.08}$ keV). The equivalent width of the 9 keV absorption profile is also stronger in 2011 compared with 2007. In contrast, the 9.5 keV absorption is consistent across both observations, while the higher energy trough above 10 keV also appears to be required in both observations (see Table 2 for details). Thus, overall the Fe *K*-band absorption appears somewhat stronger in the lower-flux 2011 observation, while the absorption profile is more extended down toward lower energies.

Table 3
Xstar Model Parameters to Iron K Absorption

Parameter	2007 Values	2011 Values
N_H[a]	$2.0^{+0.6}_{-0.5}$	[b]
$\log \xi$[c]	$3.76^{+0.12}_{-0.14}$	3.44 ± 0.06
v_{out1}[d]	$0.25 \pm 0.01c$	[b]
v_{out2}[d]	$0.29 \pm 0.01c$	[b]

Notes.
[a] Hydrogen column density in units of $\times 10^{23}$ cm^{-2}.
[b] Parameter is tied between 2007 and 2011 spectra.
[c] Log ionization parameter. The units of ξ are erg cm s^{-1}.
[d] Outflow velocity, units of c.

We investigate below a possible cause of the absorption profile variations, from fitting XSTAR photoionization models.

3.2. Line Identifications and Photoionization Models

First, we reconsider the possible identification of the absorption lines at 9 and 9.5 keV. As also discussed by R09, if the lines are identified with the $1s - 2p$ transition of Fe XXVI, then this implies a blueshift of $v_{out} = 0.25$–$0.30c$ or higher still if the lines are less ionized (He-like or lower). However, there are few other likely strong transitions in the 9–9.5 keV band that could otherwise account for the absorption, without a strong velocity shift. Indeed, the closest transition from iron is the higher-order $1s - 5p$ line of Fe XXVI at 8.91 keV, which leads to a series of higher-order ($1s - np$, where $n > 5$) lines up until the Fe XXVI edge at 9.277 keV. However, the higher-order lines will usually be substantially weaker than the transitions up to lower energy levels, unless the lines are on the saturated part of the curve of growth, which can occur at low turbulence velocities. Thus, at zero (or low) velocity shift, the stronger $1s - 2p$ (6.97 keV) and $1s - 3p$ (8.25 keV) lines of Fe XXVI should be apparent in Figure 3, which is not the case. We demonstrate this below when we fit the absorption with a self-consistent grid of photoionized absorber models.

Alternatively, there could be some weaker contribution from other higher redshift elements, namely Co, Ni, and Zn, but these are all substantially underabundant astrophysically compared with Fe, i.e., Zn and Co are 1000 times less abundant than Fe (Grevesse & Sauval 1998) and would be undetectable with the current instruments. Ni is somewhat more abundant (but still typically 20 times lower than Fe), however only higher-order H- or He-like lines of Ni are expected in the 9–9.5 keV band. Furthermore, in a recent study of iron K absorption with *Suzaku*, (Gofford et al. 2013) found that the effect of Ni was negligible on the Fe *K*-band spectra computed by XSTAR. Thus, considering all these possible alternate identifications for the absorption, the $1s - 2p$ resonance absorption lines from iron seem to be the most plausible identification.

The absorption profiles were fit with a grid of photoionization models generated by the XSTAR code v2.2 (Kallman et al. 2004). The absorption grid was generated with a turbulence velocity of $\sigma = 5000$ km s^{-1}, a power-law continuum of photon index $\Gamma = 2.2$, and was calculated from 0.10–20 keV with 10000 energy bins. The abundances used are from the solar values of Grevesse & Sauval (1998).

The absorption grid provides an excellent fit to the Fe K absorption in both observations of PDS 456 with column density $N_H = 2.0^{+0.6}_{-0.5} \times 10^{23}$ cm^{-2} and an overall fit statistic over the 2–10 keV band of $\chi^2_\nu = 224.1/221$; see Table 3 for absorber parameters. Two outflowing zones are required, with outflow

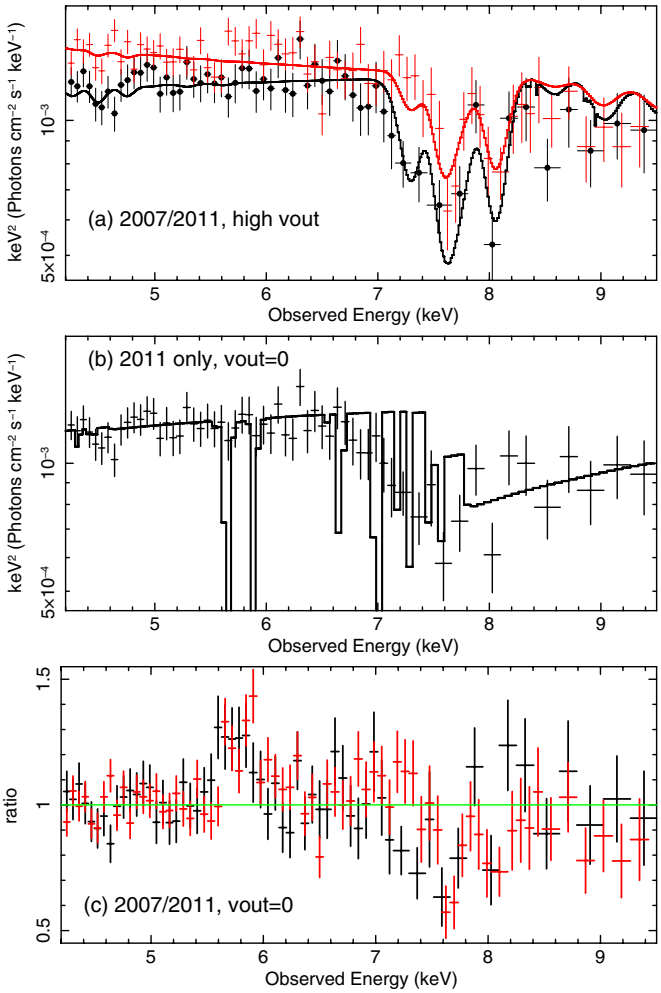

Figure 4. XSTAR fits to the Fe *K*-band absorption profile in PDS 456, as described in Section 4.1. Panel (a) shows the best-fit model with a high outflow velocity ($v_{out} = 0.25$–$0.29c$) and XSTAR turbulence of $\sigma = 5000$ km s^{-1}. Panel (b) shows the best-fit case for zero velocity shift and low turbulence ($\sigma = 100$ km s^{-1}). Only the 2011 data are shown for clarity. Panel (c) shows the ratio of the low-velocity model to the 2007 and 2011 data. The 2007 data are shown as red points and the 2011 data are shown as black points, while models are shown as solid lines. Note the plots (a) and (b) were plotted by creating fluxed spectra against a simple $\Gamma = 2$ power law and then overlaying the absorption model.
(A color version of this figure is available in the online journal.)

velocities of $v_{out} = 0.25 \pm 0.01c$ and $v_{out} = 0.29 \pm 0.01c$, which can account for the two absorption troughs at 9.0 keV and 9.5 keV, respectively. Note that the column density and outflow velocities were tied to the same values between the two observations; if they are allowed to vary, then the values are formally consistent at the 90% level. However, there is some evidence for variability of the ionization parameter between the two observations; in the lower-flux 2011 observation, the absorber is less ionized ($\log \xi = 3.44 \pm 0.06$) versus the 2007 observation ($\log \xi = 3.77^{+0.12}_{-0.14}$). If instead the ionization parameter is held fixed between the observations, then the fit statistic is subsequently worse, by $\Delta\chi^2 = 18.5$ for 1 degree of freedom. Thus, it may be the case that the lower ionization species of iron (He-like and lower) contribute to the lower energy profile of the absorption in 2011. This is shown in Figure 4(a), where the fit with a high turbulence grid ($\sigma = 5000$ km s^{-1}) and large velocity shift is shown and the extended lower-energy absorption trough can be seen toward the 2011 observation.

Next, the case where the absorption could be modeled with a zero (or small) velocity shift was investigated. In this scenario,

an absorption grid with low turbulence velocity $\sigma = 100\,\mathrm{km\,s^{-1}}$ was used. In principle, this means that for high column densities some of the usually weaker higher-order transitions are of similar strength to the lower-order ones, as the absorption lines lie on the saturated part of the curve of growth (i.e., the opposite of the high turbulence model). The velocity shift of the absorber was assumed to be zero. This resulted in a substantially worse fit when applied to both the 2007 and 2011 spectra, with a fit statistic of $\chi^2_\nu = 346.3/223$ (versus 224.1/221 for the high-velocity case), which is rejected with a null probability of 2.2×10^{-7}. The resulting fit and data/model residuals are shown in panels (b) and (c) of Figure 4. The column density obtained is very high, indeed only a lower limit can be obtained of $N_{\rm H} > 2.4 \times 10^{24}$ cm^{-2}, implying any such gas would be Compton thick to electron scattering. Similar to the high-velocity case discussed above, the ionization parameter appears to decrease from $\log \xi > 4.3$ in 2007 to $\log \xi = 3.65 \pm 0.20$ in 2011.

It is clear that the zero outflow velocity absorption profile is a poor fit to the data in both the 2007 and 2011 spectra. In particular, the zero velocity model predicts strong $1s - 2p$ absorption lines from He- and H-like iron at 6.70 and 6.97 keV, respectively (or 5.6–5.9 keV observed frame), which are not present in either data set. This produces an apparent excess in the data/model ratio residuals in panel (c) of Figure 4, where the data points are subsequently underpredicted by the model at those energies. Furthermore, the absorption profile at higher energies is also inadequately modeled by the blend of narrow, high-order transitions of iron, as is apparent in the residuals.

Thus, both data sets require absorption from highly ionized species of iron at high outflow velocities, at high statistical confidence. However, there do appear to be subtle changes in the absorption profile between 2007 and 2011, which may be accounted for by a decrease in ionization in the lower-flux 2011 observation.

4. MODELING THE SPECTRAL VARIABILITY

Having established the robustness of the high-velocity outflow in PDS 456, we next discuss models to account for the broadband spectral variability between the 2007 and 2011 observations. In particular, we consider three scenarios: (1) a simple variable intrinsic continuum, (2) models involving variable partial covering absorption (e.g., Turner et al. 2010), or (3) models involving Compton reflection (Ross & Fabian 1993; García et al. 2011). The spectra are also discussed in terms of some of the latest radiatively driven disk-wind models, i.e., using the two-dimensional (2D) radiative transfer model of Sim et al. (2008). To model the spectral variability between the two data sets, we retain the high-ionization, high-velocity absorber as described in the previous section (with parameters $N_{\rm H}$, $v_{\rm out}$, and $\log \xi$ allowed to vary). The continuum itself is modeled by a power law of variable normalization and Γ, however the photon index is assumed not to vary between the observations, except in the variable continuum scenario discussed below. A Gaussian emission line is also required at 0.9 keV, as noted previously (R09) and is included at constant intensity between observations in all the fits below. The XIS data are modeled over the energy range from 0.6–10 keV.

4.1. Intrinsic Continuum Variations

Before we consider more complex models for the spectral variability involving absorption or reflection, we tested a simple model whereby the primary photon index of the continuum (along with its normalization) varies. Such a scenario may be related to changes in the Comptonizing electron population responsible for the hard X-ray power law (e.g., Haardt & Maraschi 1991). No other additive (emission) or multiplicative (absorption) components were included, other than the 0.9 keV emission line, the high-ionization iron K absorber, and Galactic absorption. In this scenario, the intrinsic continuum does appear harder in the 2011 observation, varying from $\Gamma = 2.35 \pm 0.02$ (2007) to $\Gamma = 1.84 \pm 0.02$ (2011), while the continuum flux varies as per Table 1. However, such a simplistic change results in a statistically poor fit, with $\chi^2_\nu = 606.4/308$, which is rejected at a very high confidence level of 1.1×10^{-21}.

4.2. Partial Covering Models

Thus, in order to successfully account for the variability between 2007 and 2011, we investigated models involving gas that reprocess X-rays, either from matter that partially obscures and absorbs the AGN emission or via models that scatter and reflect X-rays off Compton-thick matter (see Section 4.3). Partial covering models have been successfully invoked many times to explain complex spectral behavior in AGNs, e.g., see Turner & Miller (2009) for a review of the phenomenon. For instance, to account for pronounced continuum curvature below 10 keV or absorption in the iron K band (e.g., Tanaka et al. 2004; Turner et al. 2005; Reeves et al. 2005; Miller et al. 2008), spectral variability and X-ray occultation (e.g., Risaliti et al. 2005; Turner et al. 2008, 2011; Behar et al. 2010; Lobban et al. 2011; Nardini & Risaliti 2011; Miyakawa et al. 2012), or pronounced hard excesses above 10 keV (e.g., Reeves et al. 2009; Risaliti et al. 2009a; Turner et al. 2010; Tatum et al. 2013). Partial covering scenarios usually require compact clouds of gas or inhomogeneous structure within the X-ray absorber, whose size scales are similar to the typical extent of the X-ray emission region. Such X-ray absorbing gas may exist in the form of broad line region clouds that may cause at least partial occultation of the X-ray source (e.g., Lamer et al. 2003; Risaliti et al. 2009b, 2009c) or could represent density fluctuations as part of an outflowing wind (e.g., Proga & Kallman 2004; Sim et al. 2010b).

Thus, a partial covering model was applied to the 2007 and 2011 observations. Two layers of partially covering gas are fit to the spectra, where the model can be expressed phenomenologically as

$$\mathrm{tbabs} \times \mathrm{xstar_{Fe}} \times \mathrm{pc_2} \times (\mathrm{po} + \mathrm{pc_1} \times \mathrm{po}), \quad (1)$$

where TBABS represents the interstellar medium absorption due to our Galaxy, $\mathrm{xstar_{Fe}}$ is the highly ionized outflowing absorber responsible for the iron K-shell absorption lines, and po is the power-law continuum emission. The components $\mathrm{pc_1}$ and $\mathrm{pc_2}$ represent the partial covering absorbing layers that have line-of-sight covering fractions of f_1 and f_2, respectively. The two partial covering zones are required as a higher column, mildly ionized zone (denoted as $\mathrm{pc_1}$ above) is needed to fit the spectral curvature above 2 keV, as well as a lower column neutral partial coverer (denoted as $\mathrm{pc_2}$), in order to model the absorption present in the soft X-ray band that is most pronounced in 2011. In this scenario, it is assumed that the column density remains invariant between observations, while the covering fractions, f_1 and f_2, are allowed to vary between observations.

The column density of the higher column $\mathrm{pc_1}$ zone is found to be $N_{\rm H} = (2.1 \pm 0.3) \times 10^{23}$ cm^{-2}, while the lower column

Table 4
Parameters of Partial Covering Absorption

Component	Parameter	2007 Values	2011 Values
pc1	N_H[a]	21.0 ± 2.5	[b]
	$\log \xi$[c]	<2.1	[b]
	v_{out}[d]	$(0.17 \pm 0.02)c$	[b]
	N_{abs}[e]	1.3 ± 0.2	$1.9^{+0.7}_{-0.3}$
	N_{unabs}[f]	2.4 ± 0.1	1.6 ± 0.2
	f_{cov}[g]	0.35 ± 0.05	$0.54^{+0.11}_{-0.07}$
pc2	N_H[a]	1.8 ± 0.5	[b]
	f_{cov}[g]	<0.16	$0.55^{+0.05}_{-0.03}$
Power law	Γ	$2.50^{+0.11}_{-0.04}$	[b]

Notes.
[a] Hydrogen column density, units of $\times 10^{22}$ cm^{-2}.
[b] Parameter is tied between 2007 and 2011 spectra.
[c] Log ionization parameter. The units of ξ are erg cm s^{-1}.
[d] Outflow velocity, units of c.
[e] Normalization of absorbed power law. The units are in photons cm^{-2} s^{-1} keV^{-1} at 1 keV.
[f] Normalization of unabsorbed power law. The units are in photons cm^{-2} s^{-1} keV^{-1} at 1 keV.
[g] Covering fraction of partial coverer.

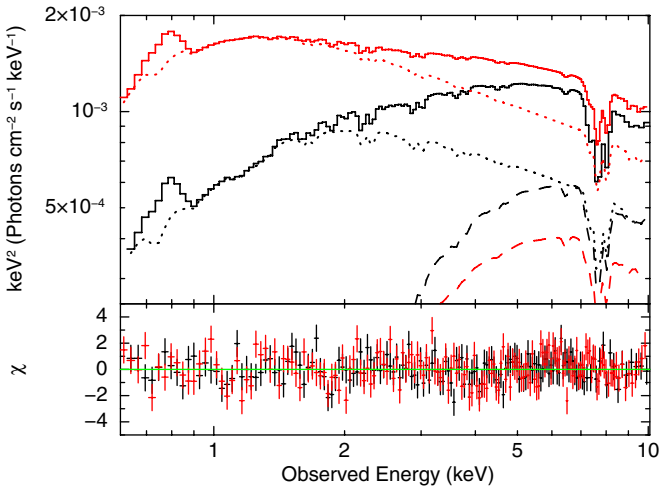

Figure 5. 2007 (red) and 2011 (black) *Suzaku* spectra fit with a partial covering model. The upper panel shows the model components, the upper solid lines show the total model emission, the dotted lines show the unabsorbed power-law continuum, and the lower dashed lines show the absorbed partially covered component. Note that the high-velocity absorber covers both continuum components. The lower panel shows the data/model residuals in units of σ. The partial covering model provides a good fit to the data, whereby the relative covering fraction of the absorbed continuum increases from 2007 and 2011.
(A color version of this figure is available in the online journal.)

pc$_2$ gas has $N_H = (1.8 \pm 0.5) \times 10^{22}$ cm^{-2}; see Table 4 for full parameter details. The differences between the two spectra can then be simply explained by an increase in the covering fraction of the partial covering absorbers from 2007 to 2011; for the high column zone, $f_1 = 0.35^{+0.04}_{-0.05}$ in 2007 increases to $f_1 = 0.54^{+0.11}_{-0.07}$ in 2011, while for the lower column zone, $f_2 < 0.16$ increases to $f_2 = 0.55 \pm 0.05$. Interestingly, some net blueshift is required for the high column zone, with $v_{out} = 0.17 \pm 0.02$c (Table 4), which may suggest that it is connected to the outflowing gas. We also note that formally this is also consistent with an absorber at $z = 0$. However, it would seem less likely that absorption associated with our own Galaxy or local group could partially cover the line of sight to a distant quasar, while the measured column density is also 100 times higher than the Galactic HI value.

Overall, the variable partial covering model provides an excellent fit to the two observations (see Figure 5), with $\chi^2_\nu = 318/302$. Note that if the N_H is also allowed to vary, then it is consistent between observations. We also note that correcting for the absorption, the X-ray luminosity of PDS 456 differs by very little between the observations, with $L_{2-10} = 4.3$–4.6×10^{44} erg s^{-1}, which favors the changes in both spectral shape and continuum flux being caused by absorber variability in this scenario.

One open question is whether partial covering is really required to explain the PDS 456 spectra. One possibility is that the low column, neutral partial covering zone (pc$_2$) instead could be described by a partially ionized (or warm) absorber, similar to those frequently observed in lower luminosity Seyfert 1 galaxies (Blustin et al. 2005; McKernan et al. 2007), which fully covers the X-ray source. In this case, the model can be expressed as

$$\text{tbabs} \times \text{xstar}_{\text{Fe}} \times \text{xstar}_{\text{WA}} \times (\text{po} + \text{pc}_1 \times \text{po}), \quad (2)$$

where xstar$_{WA}$ in Equation (2) then corresponds to the fully covering warm absorber zone, of modest ionization, which absorbs the soft X-ray spectrum below 2 keV. This description provides an excellent representation of the spectra (with $\chi^2_\nu = 325/302$). The warm absorber has a column of $N_H = 7.0^{+5.0}_{-2.0} \times 10^{21}$ cm^{-2} and ionization parameter of $\log \xi = 1.4 \pm 0.3$ during the 2011 observation, while no outflow velocity is required for this absorber. However, no such absorption is required during the softer, less absorbed 2007 observation, where the column density of the absorber is constrained to be substantially lower, with $N_H < 2.4 \times 10^{20}$ cm^{-2}.

Nonetheless, the higher column (pc$_1$) partial coverer is still required to model the spectra, while its ionization is constrained to be low ($\log \xi < 2.1$), with covering fractions as per Table 4. If this component is removed from the model and the model is refit, then the fit statistic is significantly worse with $\chi^2_\nu = 493/306$, which is rejected with a null hypothesis probability of 5.7×10^{-11}. Thus, a variable high column partial coverer would appear to be required to account for the spectral variability in PDS 456. However, one possibility is that instead of the AGN being partially covered by absorbing gas, a significant fraction of the emission could be scattered back into our line of sight from Compton-thick material.

4.3. Reflection Models

Alternatively, we investigate whether models involving X-ray reflection can account for the spectral changes, with the low flux and harder spectrum in 2011 having a higher fraction of reflected emission, as has been observed for instance through deconstruction of the time-variable spectra of Seyfert galaxies through Principal Component Analysis (e.g., Miller et al. 2007, 2008). We note the lack of a narrow 6.4 keV iron Kα line rules out a distant (e.g., pc-scale) neutral (or low-ionization) reflector, indeed the upper limits on the equivalent widths of a narrow 6.4 keV line are small; <14 eV and <28 eV respectively, for 2007 and 2011. Thus, the reflected spectrum is either required to be highly ionized or velocity broadened, as expected if it originates from the regions close to the black hole.

Thus, we replace the partial covering (pc1) component of absorption with a table of X-ray reflection spectra, using the

ionized reflection models recently computed at high resolution by (García et al. 2011), otherwise known as XILLVER. We consider the scenario whereby the reflector is highly ionized, which then results in a large degree of Compton broadening of the iron line. This then removes the requirement for additional velocity broadening of the reflection spectrum. However, in order to not overpredict the emitted soft X-ray flux, the reflection component itself is required to be absorbed by a layer of photoionized gas. Such a scenario may, to first order, replicate the reflected and absorbed emission off a disk wind (e.g., Sim et al. 2008), a possibility that we discuss further in Section 4.4. Thus, the model can be expressed as

$$\text{tbabs} \times \text{xstar}_{\text{Fe}} \times \text{xstar}_{\text{WA}} \times (\text{po} + \text{xstar}_{\text{ref}} \times \text{reflect}), \quad (3)$$

where the components are as per Equation (2), except that the reflect component represents the reflected emission, which is itself absorbed by a column of photoionized of gas ($\text{xstar}_{\text{ref}}$), with a best-fit column of $N_{\text{H}} = 2.3 \pm 0.5 \times 10^{23}$ cm^{-2} and an ionization parameter $\log \xi < 1.7$. This also provides an acceptable representation of the 2007 and 2011 spectra of PDS 456 (with $\chi^2_\nu = 328/302$). The overall model form and relative contributions of the power-law and absorbed reflection components is very similar phenomenologically to the partial covering model described in Section 4.2.

The ionization parameter of the reflector is high, $\log \xi > 4.1$, with the dominant emission occurring from H-like iron. Interestingly, there appears to be a requirement for the reflecting material to be somewhat blueshifted (or outflowing), which although the shift is poorly determined, is constrained to be at least $v_{\text{out}} > 0.11c$. This may also suggest that the reflecting material could be associated with an outflowing wind and we note that such an outflowing reflected component also appeared to be required in an analysis of the 2007 *XMM-Newton* data sets of PDS 456 by Behar et al. (2010). For the case where the bulk velocity of the reflector is forced to be zero, then the fit statistic is significantly worse by $\Delta\chi^2 = 33$. We also note that the strength of the reflected emission is relatively higher in the low-flux 2011 observation compared with the 2007 observation. Comparing the ratio (R) of the flux of the reflected component to that of the intrinsic power-law continuum in the 2–10 keV band gives a ratio of $R = 0.60 \pm 0.16$ during 2011, while in 2007 the ratio is lower with $R = 0.32 \pm 0.09$. Thus, perhaps as might be expected, the lower-flux 2011 spectrum has a relatively higher fraction of reflected flux, relative to its overall lower intrinsic continuum level.

4.4. Disk-wind Models

In the above sections, we showed that relatively ad-hoc absorption and reflection models can account for the X-ray spectral variability of PDS 456. Now, we consider whether the data can be fit self consistently via both absorption through and from reflection off the surface of an accretion disk wind. We adopt a table of synthetic spectra computed for parameterized models of smooth, steady-state, 2D biconical wind models using the radiative transfer code described by Sim et al. (2008, 2010a). The class of wind model used is described in detail in Sim et al. (2008, 2010a) and was also recently applied to the *Suzaku* spectra of six bare Seyfert 1 galaxies by Tatum et al. (2012). The computed spectra self consistently contain a combination of the radiation transmitted through the wind and reflected or scattered emission from the wind (including the iron Kα emission).

As discussed in detail by both Sim et al. (2008, 2010a) and Tatum et al. (2012), the resulting spectra are strongly dependent on the observer's orientation, which is specified by $\mu = \cos\theta$. Here, θ is the angle between the observer's line of sight and the polar z axis of the wind, with the disk lying in the xy plane, e.g., see Figure 6 for a schematic of the inner wind geometry.

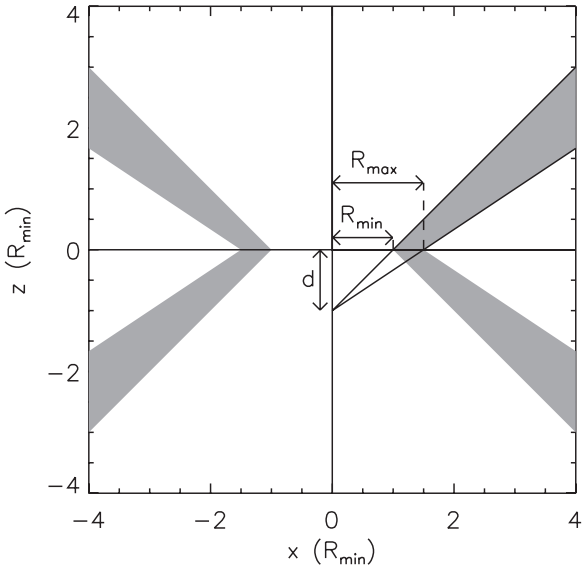

Figure 6. Disk wind geometry employed in Section 4.4, based on the model of Sim et al. (2008). The x axis represents the plane of the disk and the z axis represents the polar direction, in units of R_{min}, the minimum launch radius of the flow. The black hole is at the origin and the inclination angle is measured with respect to the z axis. The shaded area represents the physical extent of the outflow. The models presented here have $R_{\text{min}} = 32R_{\text{g}}$ along the disk plane, while the maximum launch radius $R_{\text{max}} = 1.5R_{\text{min}}$, as indicated in the figure. The d parameter is the distance of the focus point of the wind below the origin in units of R_{min} (shown for $d = 1$), as indicated by the solid lines. Therefore, increasing the d parameter makes the wind more polar. Note that only the inner part of the flow is shown for clarity and that the flow is computed out to a radius of $3.4 \times 10^4 R_{\text{g}}$.

At low values of θ (i.e., looking down at the disk plane; large values of μ), the resulting spectra have little absorption because radiation from the primary X-ray source, which is assumed to be centrally concentrated, can reach the observer directly without passing through the biconical wind structure. However, the spectra do contain a contribution from reflection off the wind surface that can produce a broadened iron K line profile. At higher values of θ (smaller values of μ), the observer sight line passes through the outflow and strong iron K absorption features can be imprinted on the spectrum. Thus, as μ is reduced, the primary continuum emission becomes increasingly suppressed by absorption and scattering processes.

Here, we adopt a grid of wind model spectra, computed for a range of wind parameters similar to those described in Tatum et al. (2012). The grid explores several variable parameters, as described below. Primary wind and X-ray source parameters used for our grid of wind models are given in Table 5 (all model other model parameters are exactly as described in Tatum et al. 2012). It is important to note that, for reasons of computational cost, our grid does not represent a systematic exploration of all of the possible parameter space of the wind model; it only varies a subset of key model parameters that act as convenient means by which to vary the typical densities, velocities, and ionization conditions in the flow. This grid is therefore useful as a starting point to investigate whether spectral features can be readily explained by a disk wind.

The grid explores a range of values for both the photon index (Γ) and luminosity (L_{X}) of the illuminating power law.

Table 5
Parameters for Disk Wind Model Grid

Parameter	Min Value	Max Value	Grid Points
$\log_{10}(\dot{M}_w/\dot{M}_{Edd})$	−0.5	−0.1	2
$\log_{10}(R_{min}/100\,R_g)$	−0.5		
$\mu = \cos\theta$	0.025	0.975	20
d/R_{min}	1	5	3
R_{max}/R_{min}	1.5		
f_v	1	2	2
Fe abundance/solar	1.0		
Γ	1.8	3.0	3
L_X/L_{Edd}	0.001	0.01	3

Notes. The parameters varied in the grid of wind models, listing minimum value, maximum value, and number of grid points, where applicable. See Section 4.4 for details of the model parameters.

Table 6
Disk Wind Model Parameters Fit to the *Suzaku* Spectrum

Parameter	Model A (2011)	Model B (2011)	Model C (2011)	Model B (2007)
f_v[a]	1	2	2	2
d[b]	1	1	2	1
$\dot{M}$[c]	0.32	0.32	0.32	0.32
L_X[d]	0.29 ± 0.08	0.34 ± 0.07	0.28 ± 0.06	>0.83
μ[e]	0.66 ± 0.02	0.42 ± 0.02	0.63 ± 0.02	0.43 ± 0.02
Γ	2.15 ± 0.05	2.05 ± 0.06	2.10 ± 0.05	2.26 ± 0.02
χ^2/dof	163.1/148	128.9/148	136.1/148	217.4/162

Notes.
[a] Model values for an escape velocity parameter one or two times the escape speed; see Section 4.4.
[b] Geometrical (collimation) factor d; see Section 4.4 for details.
[c] Mass outflow rate in units of the Eddington rate.
[d] 2–10 keV luminosity as a percentage of the Eddington luminosity.
[e] Inclination angle parameter $\mu = \cos\theta$.

The luminosity is calculated in the 2–10 keV band and is normalized as a fraction of the Eddington luminosity and thus scales independently of black hole mass. Models were computed with L_X in the range 0.1–1.0% of the Eddington luminosity. When fitting the models, the value of Γ was tied to that of the measured photon index of the spectrum, which was allowed to vary.

Spectra were calculated for two different values of the mass outflow rate of the wind ($\dot{M}$). Normalized to the Eddington accretion rate ($\dot{M}_{Edd}$), the values chosen were $\dot{M} = \dot{M}_w/\dot{M}_{Edd} = 0.32$ and 0.8, i.e., $\log_{10}(\dot{M}_w/\dot{M}_{Edd}) = -0.5$ and −0.1, respectively; see Table 5. Values of the mass outflow rate near Eddington values may be expected for PDS 456, which likely accretes at around the Eddington limit, as discussed in R09.

The terminal outflow velocities (v_∞) realized in the wind models are determined by the choice of the inner wind radius (R_{min}) and the terminal velocity parameter f_v, which is related to the terminal velocity on a wind streamline to the escape velocity at its base, via $v_\infty = f_v\sqrt{2GM_{BH}/R}$ (see Sim et al. 2008 for details). In order for the radial outflow velocities of the wind to reach high values appropriate for PDS 456, the spectral models were calculated using a fixed inner radius of the flow launching region of $R_{min} = 10^{-0.5} \times 100R_g = 32R_g$, the same as the smallest value for the inner radius considered in the Tatum et al. (2012) grid of models. A relatively low value of the outer radius for the wind launching region of $R_{max} = 1.5R_{min} = 48R_g$ was also adopted and thus R_{min} to R_{max} set the range of radii from which the wind is launched. We considered models with $f_v = 1, 2$ (i.e., terminal velocities of one or two times the escape speed from the base of the flow). The opening angles are controlled by the geometrical parameter d, which sets the degree of collimation of the wind: d is defined as the distance of the focus point of the wind below the origin. The wind geometry for the innermost part of the flow, along with the definitions of the R_{min}, R_{max}, and d parameters, are illustrated in Figure 6.

For our model grid, we considered three values for $d = 1$, 2, and 5, expressed in units of R_{min}. Here, $d = 1$ corresponds to our most equatorial wind (least collimated case) and $d = 5$ corresponds to a more polar wind (most collimated case). Solar abundances from (Asplund 2005) were used for all models. For each of our wind models, spectra were computed for 20 different values of the observer inclination parameter μ, uniformly spaced between $\mu = 0.025$ and $\mu = 0.975$. In total, our grid contains 2160 synthetic spectra.

We first apply the above models to the 2011 *Suzaku* spectrum of PDS 456, as this is the most absorbed spectrum of the two *Suzaku* observations, with a strong iron K absorption profile. Rather than let all the parameters of the wind vary simultaneously, which could lead to degeneracies in the modeling, the effect of changing different parameters on the wind model was systematically explored. Given the limited number of grid points for both parameters, values of $\dot{M}$ and f_v were fixed in each fit. However, we explored the effect of adopting the different tabulated values by changing the respective parameters in the fits and comparing the resultant χ^2. Similarly, the geometrical d parameter was also kept fixed at either $d = 1, 2$, or 5, as discussed below. The photon index of the illuminating power law was allowed to vary and was assumed to be equal to the power-law index of the measured spectrum. The inclination parameter, μ, was also allowed to vary, as was the 2–10 keV luminosity L_X, expressed as a percentage of L_{Edd}. Parameters are measured relative to the redshift of the quasar at $z = 0.184$ throughout.

The spectrum of PDS 456 was modeled with a simple power law attenuated by Galactic absorption, modified by the wind spectrum that is included in XSPEC as a multiplicative table. The spectrum was also modified by a soft X-ray warm absorber, as discussed in Section 4.2, which may originate from gas further away than the putative accretion disk wind. Alternatively, a partial covering absorber also gave an equally good fit to the soft X-ray absorption. Thus, the overall model is of the form

$$\text{tbabs} \times \text{xstar}_{WA} \times (\text{diskwind} \times \text{po}). \quad (4)$$

Initially, the spectrum was modeled with an escape speed parameter of $f_v = 1$, with $d = 1$, while the outflow rate was fixed at the lowest value of $\dot{M} = 0.32$ (in Eddington units). The models were fit over the 0.5–10 keV range of the XIS 0 and 3 combined spectrum. The resultant fit is plotted in Figure 7 (upper panel), with the resultant best-fit wind parameters and reduced χ^2 being listed in Table 6 as Model A. It can be seen that in this case that the fit to the iron line profile is quite poor, as the model fails to reproduce the entire depth or width of the profile, especially on the blueshifted side of the profile. This suggests that the velocity of the wind is not sufficiently high to match the observed profile. Note that increasing either $\dot{M}$ or d (making the outflow more polar) makes the fit even worse, in the latter case making the velocity profile shallower.

Thus, to increase the velocities, the escape velocity parameter was then increased to $f_v = 2$ in the fits, while the other parameters were kept fixed as before, i.e., $\dot{M} = 0.32$ and $d = 1$. This yields an excellent fit to the iron absorption profile (Table 6, Model B) and is plotted in Figure 7 (lower panel).

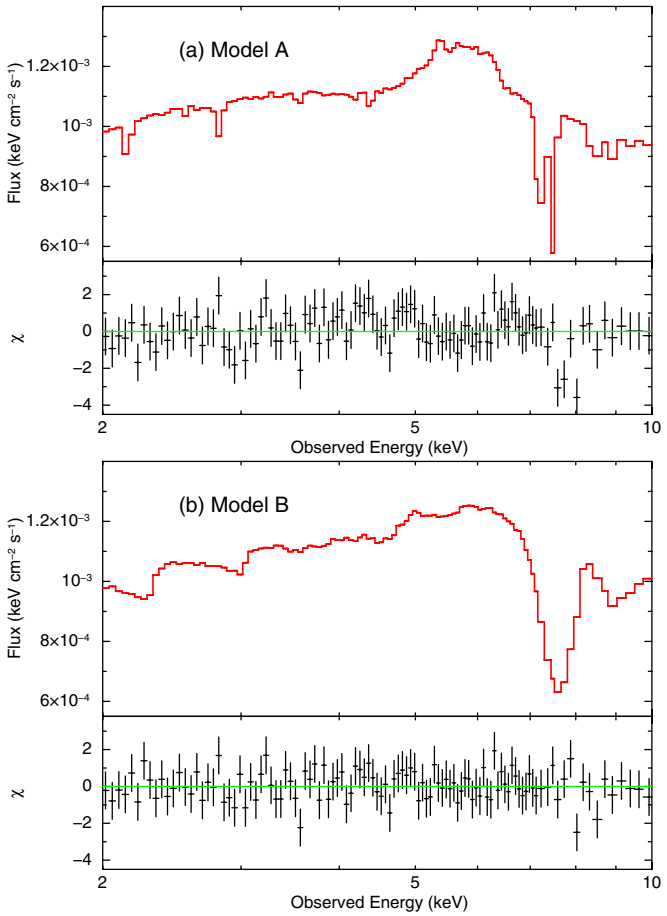

Figure 7. 2011 spectrum of PDS 456 fit with the disk-wind model of Sim et al. (2008). The upper panels show the model and the lower panels show the residuals to the fit. Models A and B show the fits with two different models, corresponding to two different values of the escape velocity parameter f_v equal to one or two times the escape velocity—see Section 4.4 for details. In each of the fits, a low inclination angle ($\mu = \cos\theta = 0.4$–0.65) is required, implying that we may be looking through the marginally Compton thick part of the wind; see Tables 5 and 6 for the model parameters.

(A color version of this figure is available in the online journal.)

Note that an equally good fit is also obtained if the outflow rate is increased to $\dot{M} = 0.8$, the main difference being that the percentage 2–10 keV luminosity increases from ∼0.3% to ∼1%. Thus, as might be expected from consideration of ionization conditions, an increase in the ionizing luminosity can be roughly compensated for by an increase in the mass outflow rate.

We also investigated the effect of increasing the collimation of the flow by increasing the d parameter to $d = 2$. This is listed as Model C in Table 6, but otherwise the parameters are the same as for Model B and the fit statistic is also similar. In this case, the model fit adjusts via the inclination parameter, which increases from $\mu = 0.42 \pm 0.02$ to $\mu = 0.63 \pm 0.02$. This also seems consistent with the fact that as the d parameter increases, the outflow becomes more polar (less equatorial) and thus the inclination angle decreases. However, we note that if the geometrical factor is increased further to $d = 5$, giving the most polar outflow, then the fit is no longer acceptable ($\Delta\chi^2 = +21.8$ with respect to Model C), as the absorption feature becomes too shallow.

Thus, in general, a moderately collimated outflow ($d = 1$–2), with a terminal velocity around twice the escape speed ($f_v = 2$) for our chosen values of R_{min} and R_{max}, appears to model well the absorption profile in PDS 456. The outflow also appears to be consistent with having a mass-loss rate close to the Eddington accretion rate. It is interesting to note that the value of the inclination parameter μ is generally low, giving $\mu = 0.4$–0.65 (or $\theta = 55$–70°). If the biconical wind geometry is correct, this would suggest that we are viewing PDS 456 at a relatively side-on inclination through the thick part of the accretion disk wind.

We caution that our grid does not explore different values for the parameters controlling the extent and location of the wind launching region (R_{min} and R_{max}). Thus, we cannot yet quantitatively comment on possible degeneracies related to the location of the wind launching region. Since the wind velocities are key to obtaining good agreement, it is to be expected that some degeneracy will exist between the choice of R_{min} and f_v (if R_{min} is reduced then a good fit may be achievable for a smaller value of f_v). While this can be explored by extending our grids of models in the future, we note that it is not expected that R_{min} is significantly smaller nor that f_v is significantly larger than the values considered here.

4.4.1. Application to the 2007 Observation

For comparison, we also applied the disk wind model described above to the 2007 *Suzaku* observation. For simplicity, Model B was adopted, with $f_v = 2$, $d = 1$, and $\dot{M} = 0.32$. As the spectrum is brighter and less absorbed, no additional soft X-ray absorption (warm absorption or partial covering) was applied to the 2007 data, thus the spectrum can be described by an intrinsic power-law like continuum modified by the presence of the disk wind. The parameters of this fit are also listed in Table 6. The inclination parameter is consistent with the 2011 model, as might be expected ($\mu = 0.43 \pm 0.02$). The only change in the model is that the X-ray luminosity increases to the maximum grid value of 1% of Eddington ($L_X > 0.83$, Table 6), while the photon index is slightly steeper ($\Gamma = 2.26 \pm 0.02$). Thus, as the 2007 observation caught PDS 456 in a higher flux state than in 2011, it would appear that the ionization state of the wind, as governed by the luminosity (L_X) of the illuminating continuum, was also correspondingly higher.

4.4.2. The Physical Conditions within the Wind

Here, we also briefly discuss some of the physical conditions within the wind model, noting however that the exact parameters are dependent upon the model that is fit and thus should just be viewed as typical estimates. We also reiterate that there are significant degeneracies among parameters of the wind model fit here, which are not adequately explored within the limited parameter space of the current model grid. For reference, however, we take the above best-fit case with the wind geometry of Model B, fit to both the 2007 and 2011 data sets, for the case of a mass outflow rate (with respect to Eddington) of $\dot{M} = 0.32$ and with inclination $\mu = 0.42$. For this model and inclination parameter, the column density through the flow along the observer's line of sight is estimated to be $N_H \sim 2 \times 10^{24}$ cm^{-2} and thus the Compton depth is of the order $\tau \sim 1$. However, the Compton depth through the flow is strongly inclination dependent, while for low values of μ the Compton depth can be reasonably high, reaching $\tau \sim 10$ for the case of $\mu = 0.05$. For face-on inclinations, the depth can be negligible, i.e., $\tau \sim 0$ for $\mu > 0.7$ (for the geometry of Model B). Figure 2 of Sim et al. (2008) demonstrates the overall effect of varying inclination on the Compton depth through the flow.

In the case of Model B, most of the absorption occurs over a physical radius of typically ∼60–160R_g. This is likely to be somewhat geometry dependent and we further note that we fixed the inner and outer radius from which the wind is launched to lie in the range 32–48R_g. However, we can take a reasonable radial scale for the wind to be of the order $R_{\rm wind} \sim 100R_g$, which for PDS 456, with an estimated black hole mass of 10^9 $M_\odot$ (R09), would correspond to a radius of $R_{\rm wind} \sim 10^{16}$ cm.

In that case, some typical physical timescales for the wind can be estimated. A simple light-crossing or reverberation timescale of the wind would be of the order $t_{\rm lc} \sim 5 \times 10^5$ s. The physical flow timescale may be somewhat (a factor of a few) longer than this, depending on the exact velocity profile of the wind, although noting that the outflow velocity predicted from the XSTAR modeling is fairly fast, of $v_{\rm out} \sim 0.25c$. In contrast, the ionization and recombination timescale of the wind may be fairly short. If, for PDS 456, we take a typical column density (depending on the exact line of sight) of $N_{\rm H} = 10^{23}$–10^{24} cm^{-2} and a radial length scale of 10^{16} cm, then the typical electron densities within the flow may be of the order of 10^7–10^8 cm^{-3}, although we note that the density in the wind will not be uniform. This could yield measurable ionization and recombination times for highly ionized iron within the outflow (e.g., for Fe XXVI) of $t_{\rm rec} \sim 10^4$–10^5 s (Seaton 1959). Such timescales are certainly well within the four yr timescale between the 2007 and 2011 observations, thus it would appear reasonable for the ionization conditions of the wind to have responded to the overall lower flux level in the 2011 observations. Subsequent on-going monitoring of the variability of the wind in PDS 456, with *Suzaku*, *XMM-Newton*, and *NuSTAR* observations in 2013–2014 will hopefully provide more insight into the variability timescales.

We can also compare the properties of the fast outflow in PDS 456, with the ultra-fast outflows typically observed in AGNs, such as those presented in Tombesi et al. (2013). From the XSTAR fits shown in Table 3, the ionization parameter is typically $\log \xi = 3.5$–4 for a column density of $N_{\rm H} = 2 \times 10^{23}$ cm^{-2}. In that case, PDS 456 lies in the typical range of the $N_{\rm H}$ versus $\log \xi$ distribution for the ultra-fast outflows presented in Tombesi et al. (2013) (see their Figure 1), while PDS 456 lies toward the higher end of the velocity distribution. This is also the case seen in comparing PDS 456 with the properties of the fast outflows detected in the *Suzaku* sample of Gofford et al. (2013). For a radial distance scale of the wind in PDS 456 of $\log(R/R_{\rm g}) \sim 2$, then according to the radial correlations in Tombesi et al. (2013), we are viewing the wind in PDS 456 along the innermost measured part of the AGN outflow (see their Figure 3 of ionization, column, or outflow velocity versus radial location in the wind). Thus, PDS 456 would appear to have the typical properties of an ultra-fast outflow, although we could be viewing the quasar through the innermost part of the disk wind.

Finally, we can make an approximate estimate for the size scale of the soft X-ray absorbing region, which can either be associated with the more typical warm absorbing regions found in Seyfert 1s (Blustin et al. 2005; McKernan et al. 2007) or with near neutral matter partially covering the X-ray source. Although no velocity information on the soft X-ray absorber is available from these data, if the velocity is similar to the typical velocities found in soft X-ray warm absorbers, ∼1000 km s^{-1}, then for a variablity timescale within four yr, the implied absorber size scale is ∼10^{16} cm. Although the estimate is very much dependent on the absorber velocity, this size scale is similar to the fast absorber associated with the accretion disk wind.

4.5. Is PDS 456 X-Ray Quiet?

One final consideration is how much the intrinsic X-ray emission in PDS 456 is suppressed by the disk wind, especially since it appears that PDS 456 may be directly viewed through the marginally Compton thick part of the flow at moderate inclination. The observed 2–10 keV luminosity of PDS 456 in 2011 is $L_{2-10} = 2.6 \times 10^{44}$ erg s^{-1}. This would make PDS 456 relatively X-ray quiet compared with bright radio-quiet quasars (Elvis et al. 1994), as the observed 2–10 X-ray luminosity is only ∼0.3% of the total bolometric luminosity of $L_{\rm bol} \sim 10^{47}$ erg s^{-1} (Simpson et al. 1999; O'Brien et al. 2005; Reeves et al. 2009). Indeed, such a low 2–10 keV luminosity is also predicted by the disk wind modeling, as the fit typically favored $L_{\rm X}$ to be typically about ∼0.3% of the Eddington luminosity, which for the estimated black hole mass of ∼10^9 $M_\odot$ (R09), is $L_{\rm Edd} \sim 10^{47}$ erg s^{-1} for PDS 456.

We note that the X-ray flux of PDS 456 is attenuated by the disk wind by a factor of two times in the models fit here, which could in part explain the X-ray weakness. Potential further attenuation of the X-ray emission could occur if shielding gas was also present in PDS 456, which is not accounted for in the Sim et al. (2008) model, but may be needed for the wind not to become overionized in the acceleration region (Murray et al. 1995). The partial covering absorber discussed in previous sections could possibly act as a source of such material if it is located near the base of the wind, which would in effect lower the X-ray luminosity that both the wind and the observer sees. PDS 456 may also be similar in this regard to broad absorption line (BAL) quasars, which are known to be X-ray weak due to absorption (Gallagher et al. 2002).

Alternatively, it may be that PDS 456 is intrinsically X-ray weak, as the observed bolometric correction for the 2–10 keV band luminosity is a factor of 300 times, much higher than in typical AGNs (Elvis et al. 1994). It is possible, however, for the 2–10 keV bolometric correction to reach values of ∼100 for Eddington-limited sources (e.g., Vasudevan & Fabian 2009) and thus AGNs like PDS 456 may therefore be intrinsically X-ray weak. Although PDS 456 is a high luminosity AGN, it may have some similarities with narrow-line Seyfert 1s (NLS1s), which can also have weak 2–10 keV emission with respect to bolometric, due to their steep X-ray photon indices (Leighly 1999). While PDS 456 has broad Balmer lines (i.e., Hβ FWHM ∼ 3500 km s^{-1}), like the NLS1s it does have weak [O III] yet strong Fe II emission (Simpson et al. 1999), while its intrinsic X-ray photon index is also steep ($\Gamma = 2.4$). Thus, PDS 456 may also be a high luminosity analog of the NLS1s, with a high Eddington ratio.

5. CONCLUSIONS

We have presented a new 2011 *Suzaku* observation of the nearby, luminous quasar PDS 456. The new observation has confirmed the detection of the iron K-shell absorption lines that were detected in the 2007 *Suzaku* observation (R09) at ∼9 keV in the quasar rest frame. Indeed, the possibility of highly blueshifted absorption in PDS 456 was first suggested by Reeves et al. (2003) as evidence for a fast, powerful wind. We have shown that the 9 keV band absorption cannot be modeled with an absorber with zero (or small) outflow velocity and instead is best modeled by highly blueshifted lines from Fe XXV-XXVI, with an outflow velocity of 0.25–0.29c. This makes PDS 456 one of the fastest high-velocity outflows known, compared with those

detected in recent X-ray samples (Tombesi et al. 2010; Gofford et al. 2013), which tend to cover the range from 0.01–0.30c.

The overall X-ray spectrum of PDS 456 in 2011 also appears to be harder and observed at an lower overall flux, compared with the 2007 observation. This spectral variability could not simply be accounted for by a simple change in continuum level and photon index between the observations. The differences between the two observations can be explained by variations in the line-of-sight covering fraction of a partial covering absorber. This interpretation has also been favored to explain the X-ray spectral variability of several type I AGNs, which can sometimes display low and hard absorbed spectra, which may be due to partial occultation by absorbing clouds (e.g., Risaliti et al. 2005; Turner et al. 2008, 2011; Behar et al. 2010; Lobban et al. 2011; Nardini & Risaliti 2011; Miyakawa et al. 2012; Pounds & King 2013). Alternatively, the 2011 spectrum may also contain a higher fraction of reprocessed and scattered X-ray emission, for instance off the surface of an accretion disk wind.

Indeed, we have shown that the strongly blueshifted Fe K-band absorption in PDS 456 can be produced by a simple smooth 2D parameterization of an accretion disk wind (Sim et al. 2008). In PDS 456, it may appear that we are viewing the quasar at relatively low inclination through at least a marginally Compton thick part of an accretion disk wind, which can also explain the absorbed nature of the X-ray spectrum, especially at a lower flux during 2011. PDS 456 also shows characteristics similar to BAL quasars and is also X-ray weak, which may be accounted for by enhanced X-ray absorption toward the quasar. The iron K-band outflow velocity of PDS 456 is also similar to the X-ray outflow velocity measured in the well-studied BAL quasar APM 08279+5255 at $z = 3.97$ (Chartas et al. 2002). Interestingly, an earlier UV snapshot spectrum of PDS 456 (O'Brien et al. 2005), with the *Hubble Space Telescope HST*/STIS, revealed the possibility of broad absorption troughs, e.g., at the Lyα line, as well as a highly blueshifted C IV emission profile. Further upcoming spectroscopy with *HST*/Cosmic Origins Spectrograph will hopefully shed light on the possible UV BAL-like features in PDS 456.

Generally, accretion disk-driven winds appear to be a promising starting point to explain the increasing number of ultra-fast outflows now been observed in AGN X-ray spectra (Tombesi et al. 2010, 2011; Gofford et al. 2013). Such profiles, such as the smooth 2D wind model of Sim et al. (2008), can also self consistently explain their iron line emission profiles as well as absorption and can reproduce an apparent P-Cygni-like profile, as measured for instance in PG 1211+143 (Pounds & Reeves 2009; Sim et al. 2010a). Disk winds models can also plausibly reproduce the broad iron lines of some Seyfert 1s, through reflection off the wind surface (Tatum et al. 2012). In order to accurately quantify such winds, more realistic geometries (likely including sub-structure/clumping) need to be explored, as well as time variability in the flow; indeed, a radiatively driven AGN disk wind might be expected to display complex time dependence (Proga et al. 2000; Proga & Kallman 2004). Further deep observations of PDS 456, scheduled with *Suzaku* and *XMM-Newton* during 2013, will further explore the short timescale variability of the wind spectrum. In the future, iron K absorption profiles will be revealed with unprecedented resolution with the Soft X-ray Spectrometer calorimeter onboard Astro-H.

J.N.R. acknowledges financial support from STFC and Chandra grant number GO1-12143X. T.J.T. acknowledges NASA grant number NNX11AJ57G. We would like to thank Javier Garcia for the use of his XILLVER reflection model. This research has made use of data obtained from the *Suzaku* satellite, a collaborative mission between the space agencies of Japan (JAXA) and the United States (NASA).

REFERENCES

Asplund, M. 2005, ARA&A, 43, 481
Behar, E., Kaspi, S., Reeves, J., et al. 2010, ApJ, 712, 26
Blustin, A. J., Page, M. J., Fuerst, S. V., Branduardi-Raymont, G., & Ashton, C. E. 2005, A&A, 431, 111
Chartas, G., Brandt, W. N., & Gallagher, S. C. 2003, ApJ, 595, 85
Chartas, G., Brandt, W. N., Gallagher, S. C., & Garmire, G. P. 2002, ApJ, 579, 169
Dickey, J. M., & Lockman, F. J. 1990, ARA&A, 28, 215
Di Matteo, T., Springel, V., & Hernquist, L. 2005, Natur, 433, 604
Elvis, M., Wilkes, B. J., McDowell, J. C., et al. 1994, ApJS, 95, 1
Fukazawa, Y., Mizuno, T., Watanabe, S., et al. 2009, PASJ, 61, S17
Fukumura, K., Kazanas, D., Contopoulos, I., & Behar, E. 2010, ApJ, 715, 636
Gallagher, S. C., Brandt, W. N., Chartas, G., & Garmire, G. P. 2002, ApJ, 567, 37
García, J., Kallman, T. R., & Mushotzky, R. F. 2011, ApJ, 731, 131
Gofford, J., Reeves, J. N., Tombesi, F., et al. 2013, MNRAS, 430, 60
Grevesse, N., & Sauval, A. J. 1998, SSRv, 85, 161
Gruber, D. E., Matteson, J. L., Peterson, L. E., & Jung, G. V. 1999, ApJ, 520, 124
Haardt, F., & Maraschi, L. 1991, ApJL, 380, L51
Kalberla, P. M. W., Burton, W. B., Hartmann, D., et al. 2005, A&A, 440, 775
Kallman, T. R., Palmeri, P., Bautista, M. A., Mendoza, C., & Krolik, J. H. 2004, ApJS, 155, 675
Kato, Y., Mineshige, S., & Shibata, K. 2004, ApJ, 605, 307
Kazanas, D., Fukumura, K., Behar, E., Contopoulos, I., & Shrader, C. 2012, AstRv, 7, 92
King, A. R. 2003, ApJL, 596, L27
King, A. R., & Pounds, K. A. 2003, MNRAS, 345, 657
Koyama, K., Tsunemi, H., Dotani, T., et al. 2007, PASJ, 59, 23
Lamer, G., Uttley, P., & McHardy, I. M. 2003, MNRAS, 342, L41
Leighly, K. M. 1999, ApJS, 125, 317
Lobban, A. P., Reeves, J. N., Miller, L., et al. 2011, MNRAS, 414, 1965
McKernan, B., Yaqoob, T., & Reynolds, C. S. 2005, MNRAS, 361, 1337
McKernan, B., Yaqoob, T., & Reynolds, C. S. 2007, MNRAS, 379, 1359
McQuillin, R. C., & McLaughlin, D. E. 2012, MNRAS, 423, 2162
Miller, L., Turner, T. J., Reeves, J. N., et al. 2007, A&A, 463, 131
Miller, L., Turner, T. J., & Reeves, J. N. 2008, A&A, 483, 437
Mitsuda, K., Bautz, M., Inoue, H., et al. 2007, PASJ, 59, 1
Miyakawa, T., Ebisawa, K., & Inoue, H. 2012, PASJ, 64, 140
Murray, N., Chiang, J., Grossman, S. A., & Voit, G. M. 1995, ApJ, 451, 498
Nardini, E., & Risaliti, G. 2011, MNRAS, 417, 2571
O'Brien, P. T., Reeves, J. N., Simpson, C., & Ward, M. J. 2005, MNRAS, 360, L25
Pounds, K. A., & King, A. R. 2013, MNRAS, 433, 1369
Pounds, K. A., & Reeves, J. N. 2009, MNRAS, 397, 249
Pounds, K. A., Reeves, J. N., King, A. R., et al. 2003, MNRAS, 345, 705
Proga, D., & Kallman, T. R. 2004, ApJ, 616, 688
Proga, D., Stone, J. M., & Kallman, T. R. 2000, ApJ, 543, 686
Reeves, J. N., O'Brien, P. T., Braito, V., et al. 2009, ApJ, 701, 493
Reeves, J. N., O'Brien, P. T., Vaughan, S., et al. 2000, MNRAS, 312, L17
Reeves, J. N., O'Brien, P. T., & Ward, M. J. 2003, ApJL, 593, L65
Reeves, J. N., Pounds, K., Uttley, P., et al. 2005, ApJL, 633, L81
Risaliti, G., Bianchi, S., Matt, G., et al. 2005, ApJL, 630, L129
Risaliti, G., Braito, V., Laparola, V., et al. 2009a, ApJL, 705, L1
Risaliti, G., Miniutti, G., Elvis, M., et al. 2009b, ApJ, 696, 160
Risaliti, G., Salvati, M., Elvis, M., et al. 2009c, MNRAS, 393, L1
Ross, R. R., & Fabian, A. C. 1993, MNRAS, 261, 74
Seaton, M. J. 1959, MNRAS, 119, 81
Silk, J., & Rees, M. J. 1998, A&A, 331, L1
Sim, S. A., Long, K. S., Miller, L., & Turner, T. J. 2008, MNRAS, 388, 611
Sim, S. A., Miller, L., Long, K. S., Turner, T. J., & Reeves, J. N. 2010a, MNRAS, 404, 1369
Sim, S. A., Proga, D., Miller, L., Long, K. S., & Turner, T. J. 2010b, MNRAS, 408, 1396
Simpson, C., Ward, M., O'Brien, P., & Reeves, J. 1999, MNRAS, 303, L23
Takahashi, T., Abe, K., Endo, M., et al. 2007, PASJ, 59, 35

Tanaka, Y., Boller, T., Gallo, L., Keil, R., & Ueda, Y. 2004, PASJ, 56, L9
Tatum, M. M., Turner, T. J., Miller, L., & Reeves, J. N. 2013, ApJ, 762, 80
Tatum, M. M., Turner, T. J., Sim, S. A., et al. 2012, ApJ, 752, 94
Tombesi, F., Cappi, M., Reeves, J. N., et al. 2010, A&A, 521, A57
Tombesi, F., Cappi, M., Reeves, J. N., et al. 2013, MNRAS, 430, 1102
Tombesi, F., Sambruna, R. M., Reeves, J. N., Reynolds, C. S., & Braito, V. 2011, MNRAS, 418, L89
Torres, C. A. O., Quast, G. R., Coziol, R., et al. 1997, ApJL, 488, L19
Turner, T. J., Kraemer, S. B., George, I. M., Reeves, J. N., & Bottorff, M. C. 2005, ApJ, 618, 155
Turner, T. J., & Miller, L. 2009, A&ARv, 17, 47
Turner, T. J., Miller, L., Kraemer, S. B., & Reeves, J. N. 2011, ApJ, 733, 48
Turner, T. J., Miller, L., Reeves, J. N., et al. 2010, ApJ, 712, 209
Turner, T. J., Reeves, J. N., Kraemer, S. B., & Miller, L. 2008, A&A, 483, 161
Vasudevan, R. V., & Fabian, A. C. 2009, MNRAS, 392, 1124
Wilms, J., Allen, A., & McCray, R. 2000, ApJ, 542, 914